Article

Improved Corrosion Properties of Mg-Gd-Zn-Zr Alloy by Micro-Arc Oxidation

Xue Geng [1], Qiangsheng Dong [1,2] and Xiaobo Zhang [1,2,*]

1   School of Materials Science and Engineering, Nanjing Institute of Technology, Nanjing 211167, China
2   Jiangsu Key Laboratory of Advanced Structural Materials and Application Technology, Nanjing 211167, China
*   Correspondence: xbzhang@njit.edu.cn

Abstract: In order to improve the corrosion resistance of Mg-3Gd-1Zn-0.4Zr (GZ31K) alloys for biomedical application, the alloy was micro-arc oxidation (MAO)-treated using silicate electrolyte system under various voltages (400 V, 425 V, 450 V, 475 V). The effects of voltage on the microstructure and corrosion properties of MAO coating were investigated via X-ray diffraction (XRD) and a scanning electron microscope (SEM) combined with an energy-dispersive spectrometer (EDS), X-ray photoelectron spectroscope (XPS), and electrochemical experiments. The results showed that, with the increase in voltage, the MAO coatings became thicker and the micropores on the MAO coating increased in diameter. The main phase compositions of the MAO coatings were MgO and Mg_2SiO_4. Potentiodynamic polarization curve results showed that MAO coatings could enhance corrosion resistances, where the corrosion current density decreased by six orders of magnitude and the corrosion potential of the specimens increased by 300 mV for the voltage of 450 V in the MAO treatment; nevertheless, the corrosion resistance rapidly deteriorated due to the creation of large micropores in the MAO coating, which provide a pathway for corrosive media when the voltage is 475 V. The electrochemical impedance spectroscopy results showed that MAO treatments could increase low-frequency modulus resistance and increase the corrosion resistance of Mg alloys. In addition, MAO-treated GZ31K alloys still exhibited uniform corrosion, which is desirable for biomedical applications.

Keywords: magnesium alloy; micro-arc oxidation; voltage; corrosion behavior; uniform corrosion

1. Introduction

Magnesium (Mg) alloys are widely used as medical implant materials due to the advantages of their good mechanical properties, degradability, and biocompatibility [1,2]. However, the poor chemical stability, uneven corrosion, and poor corrosion resistance of Mg alloys greatly limit their applications [3]. Therefore, it is of great significance to develop biomedical Mg alloys with a high corrosion resistance and uniform corrosion mode for clinical application.

At present, micro-arc oxidation (MAO) is an effective method to slow down the degradation rate of Mg alloys, with the dual functions of adjusting the degradation rate and improving biocompatibility [4]. However, the performance of the coating during MAO will be affected by various factors, such as its electrolyte characteristics, electrical parameters, and matrix composition. In particular, the film thickness and corrosion resistance are very sensitive to the process parameters, which significantly affect the comprehensive service performance of Mg alloys [5,6]. MAO technology has the advantages of a high treatment efficiency, strong bonding between the film and the substrate, and good corrosion resistance [7–10]. It has been reported that MAO can provide a protective barrier between Mg alloys and corrosive media, and the oxide layer grows in situ on the surface of Mg alloys, thus acting as a passivation and improving their corrosion resistance [5,11]. However, there are some inherent defects in MAO coatings, including micropores and microcracks [12,13],

through which corrosive media can penetrate and contact the Mg matrix [14–16]. Moreover, the higher pore density on the surface of MAO coatings increases their effective surface area, which increases the tendency of the corrosive media to be adsorbed and concentrated in the pores, and thus reduces the corrosion resistance of MAO coatings [17].

However, surface treatment does not fundamentally solve the problem of localized corrosion [17,18]. It has been shown that if an alloy itself exhibits localized corrosion, it still presents localized corrosion after MAO, NaOH, or fluoride treatments [19,20], which is harmful to the mechanical integrity of the implant and can easily lead to premature failure. Therefore, biodegradable Mg alloys with a homogeneous corrosion behavior are desired.

The Mg-Gd-Zn-Zr alloy has many advantages, such as good comprehensive mechanical properties, good biocompatibility, a low corrosion rate, and a uniform corrosion mode [21,22]. In this work, the uniformly corroded Mg-3Gd-1Zn-0.4Zr (GZ31K) alloy was used as the research object to study the influence of different voltages (400 V, 425 V, 450 V, 475 V) of MAO treatment on the corrosion behavior of the coating on the alloy, including the corrosion resistance and corrosion mode. After MAO, the Mg alloy still showed uniform corrosion, indicating that it has good application prospects in biodegradable implantation applications.

2. Experimental

The Mg-3Gd-1Zn-0.4Zr (GZ31K) alloy was prepared using the gravity-casting method; samples with diameter of 14 mm and thickness of 3.8 mm were cut for microstructure observation and corrosion tests. The non-inductive steel tank was used as the cathode in the micro-arc reaction with a circulating cooling system, and the Mg alloy was used as the anode. It has been reported that the anodizing is shortened in this voltage range, the MAO coating grows quickly, and the thickness is uniform [23,24]. A study has shown that when the voltage is less than 450 V, the thickness of the film increases slightly with the increase in voltage; when the voltage is greater than 450 V, the thickness of the film increases significantly with the increase in voltage, and the thickness of the film will greatly affect the corrosion resistance of the alloy; and as the applied voltage rises from 400 V to 500 V, the surface porosity will be relatively stable [25]. Therefore, the voltage for MAO was set to 400 V, 425 V, 450 V, and 475 V in this work. When the voltage reaches the set value, the experiment ends. A large white spark is generated during the experiment, and as the voltage increases, the spark becomes more flickering. The main electrical parameters were the current density of 0.2 A/cm^2, the positive duty cycle of 30%, and the pulse frequency of 500 Hz. The alkaline electrolyte was mixed with 20 g/L $Na_2SiO_3 \cdot 9H_2O$, 2 g/L NaOH and 4 g/L $KF \cdot 2H_2O$.

The structure and morphology of the MAO coating were characterized by scanning electron microscope (SEM, JSM-6360LV, JEOL, Tokyo, Japan) and a field emission scanning electron microscope (MERLIN Compact, ZEISS, Oberkochen, Germany) equipped with an energy-dispersive X-ray spectroscope (EDS, Oxford Atec X-max 50, Oxford Company, Oxford, UK). The coatings were gold-sprayed prior to SEM observation. The average micropore size of the alloys was calculated by Image-Pro Plus software (Image-Pro Plus 6.0, Kebai Biotechnology, Nanjing, China).

X-ray diffraction (XRD, Ultima-IV, Rigaku, Tokyo, Japan) was used to analyze the phase composition of the MAO coating, and the XRD curves were calibrated using MDI Jade 6.5 software and standard PDF cards. The diffraction matrix was a copper target, the electron accelerating voltage was 40 kV, and the XRD was carried out by swept-angle incidence scanning, in which the incidence angle was 2.5°, the scanning speed was 5°/min, and the scanning angle was 20–80°. X-ray photoelectron spectroscopy (XPS, Nexsa, Thermo Fisher Scientific, Waltham, MA, USA) irradiated with Al Kα revealed the elemental composition and chemical state of the upper layers of different alloy compositions. Advantage 5.9931 software (Advantage, Thermo Fisher Scientific, Waltham, MA, USA) was used for data fitting.

The corrosion electrochemical behaviors of the samples in simulated body fluid (SBF; the compositions are listed in Table 1 [22]) was measured on a standard three-electrode system electrochemical workstation (PARSTAT2273, Ametek Company, Berwyn, PA, USA), in which the uncoated or coated Mg alloy with an exposed surface area of 1 cm^2 was used as working electrode, platinum electrode as auxiliary electrode, and saturated calomel electrode as the reference electrode. Electrochemical impedance spectrum (EIS) and polarization tests were conducted. Before testing, an open circuit potential was measured for 15 min to stabilize the potential. The scanning speed of the polarization curve was 1 mV/s. The amplitude of the sine wave excitation signal used in the EIS test was 10 mV, and the frequency range was 100 kHz~100 mHz. Three samples of each state were prepared for electrochemical testing, and each sample was measured once. Zview software (Zview 2, Scribner Associates Inc., Southern Pines, NC, USA) was used for data fitting for the impedance spectra.

Table 1. Compositions of the simulated body fluid (adapted from Ref. [22]).

Component	NaCl	CaCl$_2$	KCl	NaHCO$_3$	MgCl$_2$·6H$_2$O	Glucose	Na$_2$HPO$_4$·2H$_2$O	KH$_2$PO$_4$	MgSO$_4$·7H$_2$O
Concentration/g·L^{-1}	8.00	0.14	0.40	0.35	0.10	1.00	0.06	0.06	0.06

3. Results and Discussion

3.1. Microstructure

The as-cast alloy was composed of grey α-Mg, a bright eutectic phase, and lamellar structures at the outer edge of the α-Mg grains [26]. Figure 1 shows the coating surface morphologies of the GZ31K samples after MAO treatment under different voltages. It shows that some micropores become larger, the number of micropores decreases, and microcracks increase with increasing voltage. Image-pro Plus software calculations show that the average size of micropores per sample was 1.64 μm, 2.52 μm, 4.85 μm, and 5.10 μm, respectively. It is known that the discharge intensity of individual sparks increases, and more melting products are ejected from the discharge channel and rapidly deposited around the discharge channel with the increase in voltage [23]. It has been reported that the change in microporous structure with voltage is attributed to the dielectric breakdown of the MAO coating [25]. In addition, for the same electrolyte, the porosity of the MAO coating decreases with increasing voltage, and the size of the micropores increases, mainly because the micropores are filled by solids within the pores; the increase in voltage promotes the growth of the coating and the formation of a thicker coating, which makes it less likely that the plasma discharge will penetrate through the coating, thus decreasing the porosity [27]. The microcracks produced on the surface were concentrated around the micropores and interconnected, suggesting that as the oxide film was formed, the molten base alloy came into contact with the rapidly cooled electrolyte through the discharge channel, forming cracks around the pores during rapid cooling and solidification [28]. Furthermore, with the increase in applied voltage, the discharge intensity of a single spark was enhanced so that the pore size of the film increased at a higher applied voltage. The discharge spark was especially serious, as it brought about thermal stress in the coating at a higher applied voltage, and induced some cracks on the surface of coatings after solidification [29].

Figure 2 shows the cross-sectional morphologies and elemental distribution of the red lines from the MAO coating to the substrate. The MAO coating becomes thicker and more uniform with the increase in voltage. The thickness of the MAO coating obtained at 400 V, 425 V, 450 V, and 475 V is approximately 9 μm, 11 μm, 15 μm, and 30 μm, respectively, and it can be seen the coatings of the 450 V MAO group and the 475 V MAO group appear to be more tightly bound to the substrate, but the MAO coating at 400 V and 425 V is loose and more microcracks are formed at 425 V. However, it can be seen from the cross-sectional morphology that there are some small micropores in the 450 V MAO coatings, whereas larger micropores are produced in the MAO coating at 475 V. The composition distributions from the MAO coatings to the substrate, shown in yellow lines in Figure 2a–d, were tested

by EDS, and the results of the yellow lines are plotted in Figure 2(a1–d1), respectively. The main compositions of the MAO coating are Mg, Si, and O, of which Mg is mainly from the Mg matrix, and Si and O come from the electrolyte. The content of other elements is very low.
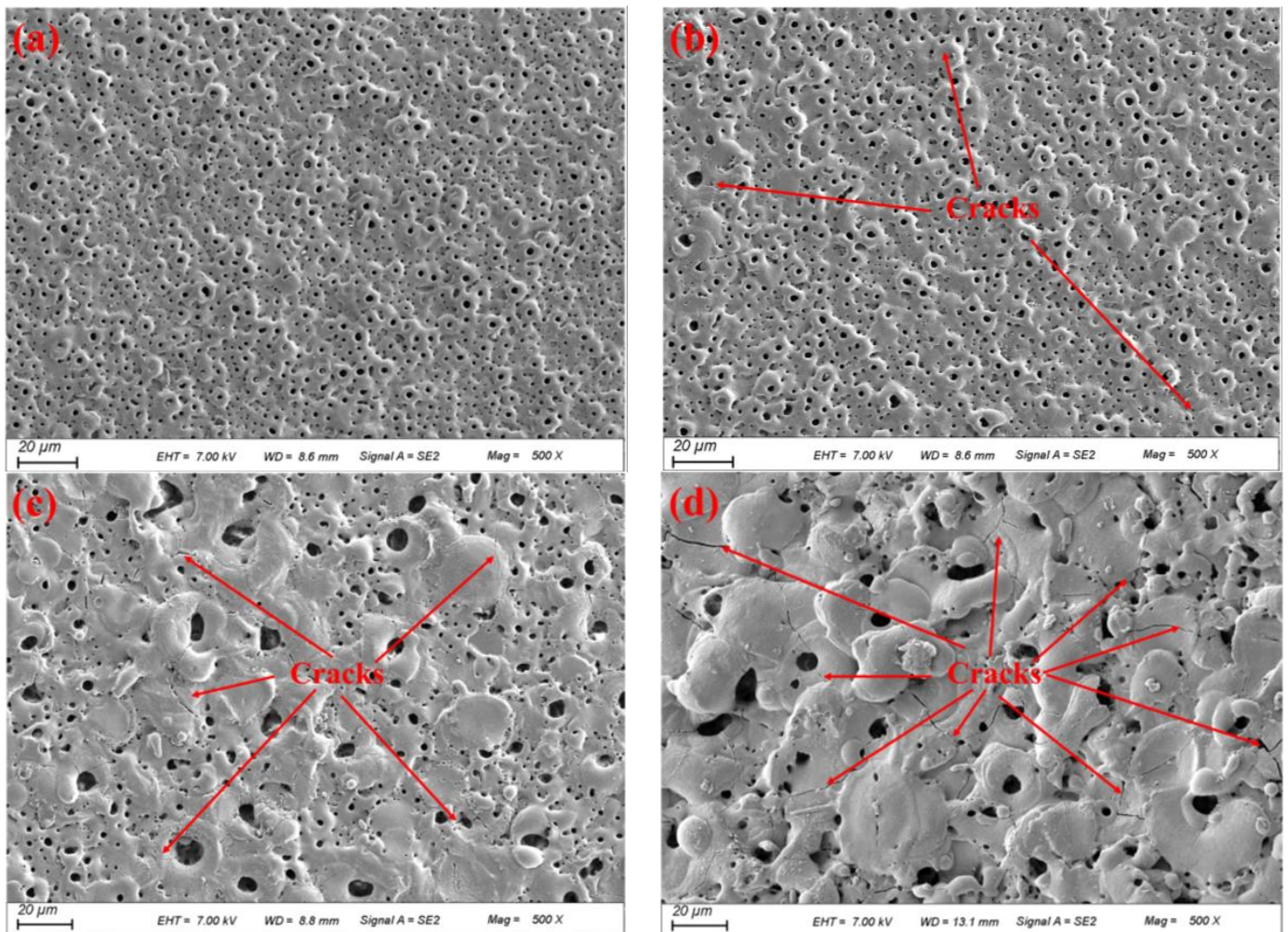

Figure 1. SEM images of the MAO coatings (**a**) 400 V, (**b**) 425 V, (**c**) 450 V, (**d**) 475 V.

To study the components of the MAO coating, the XRD patterns of the MAO coatings are shown in Figure 3. The coatings are all composed of MgO and Mg_2SiO_4. In addition, due to the thinness of the MAO coating and the existence of tiny micropores on the surface, the X-rays can easily pass through the MAO coating and impact the substrate, so strong α-Mg diffraction peaks were obtained. With the increase in voltage, the diffraction peak of MgO strengthens, indicating that the crystallinity of the film is increasing, which is because the growth of the film is affected by the increase in voltage, resulting in the direction and speed of the ion transfer being affected. Some studies have shown that the MAO coating of the silicic acid system cannot be detected by XRD experiments, which may be because Mg_2SiO_4 is in an amorphous state [30].
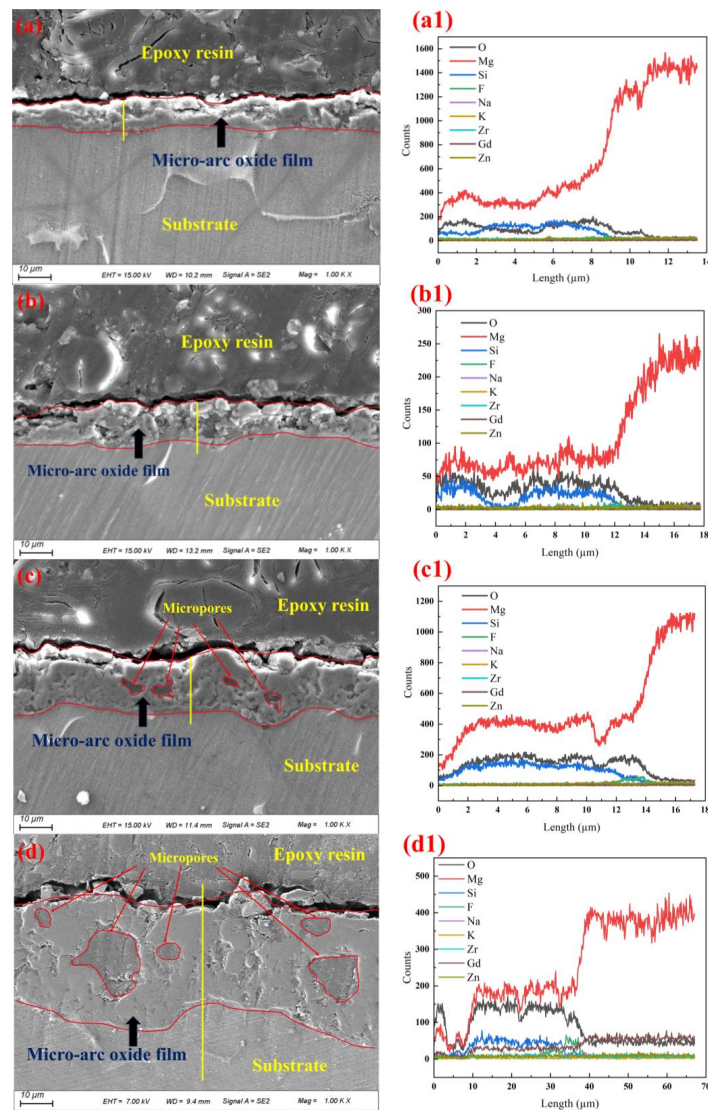
Figure 2. Cross-section morphologies and element distribution of MAO coatings (**a**,**a1**) 400 V, (**b**,**b1**) 425 V, (**c**,**c1**) 450 V, (**d**,**d1**) 475 V.
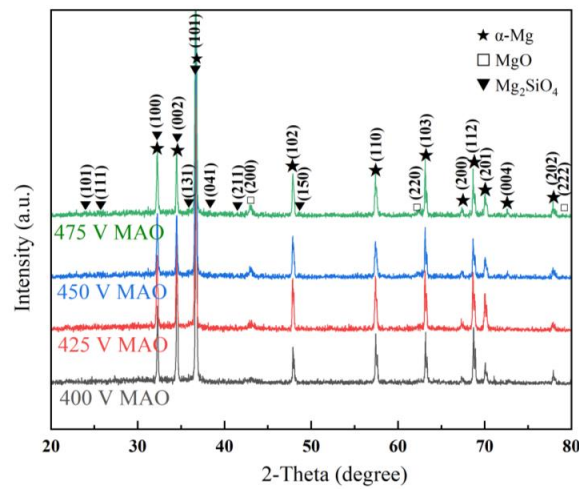

Figure 3. XRD patterns of the MAO-treated alloy.

In order to further analyze the chemical composition of the MAO coating, an XPS analysis was carried out. Figure 4 shows the full spectrum of XPS and the high-resolution XPS spectrum of the Mg 1s, O 1s and Si 2p of 450 V MAO alloys. Figure 4a shows that the broad spectrums confirm that the MAO coating consisted of Mg, O, Si, Na, and F elements. The narrow spectrums of Mg 1s, O1s, and Si 2p are listed in Figure 4b–d. Two components of MgO (1303.9 eV) and Mg_2SiO_4 (1304.6 eV) were present in the MAO coating (Figure 4b). The O 1s the narrow spectrum of the MAO coating, which also included MgO (531.3 eV) and Mg_2SiO_4 (532.3 eV) (Figure 4c); the Si 2p peak occurs at a binding energy of 102.6 eV, which is consistent with the presence of Mg_2SiO_4 [31] (Figure 4d). By using Advantage software, the area ratio of the fitting peaks of MgO and Mg_2SiO_4 was found to be 1.49; the area ratio is the ratio of content. This revealed the presence of MgO and Mg_2SiO_4 in the MAO coating.
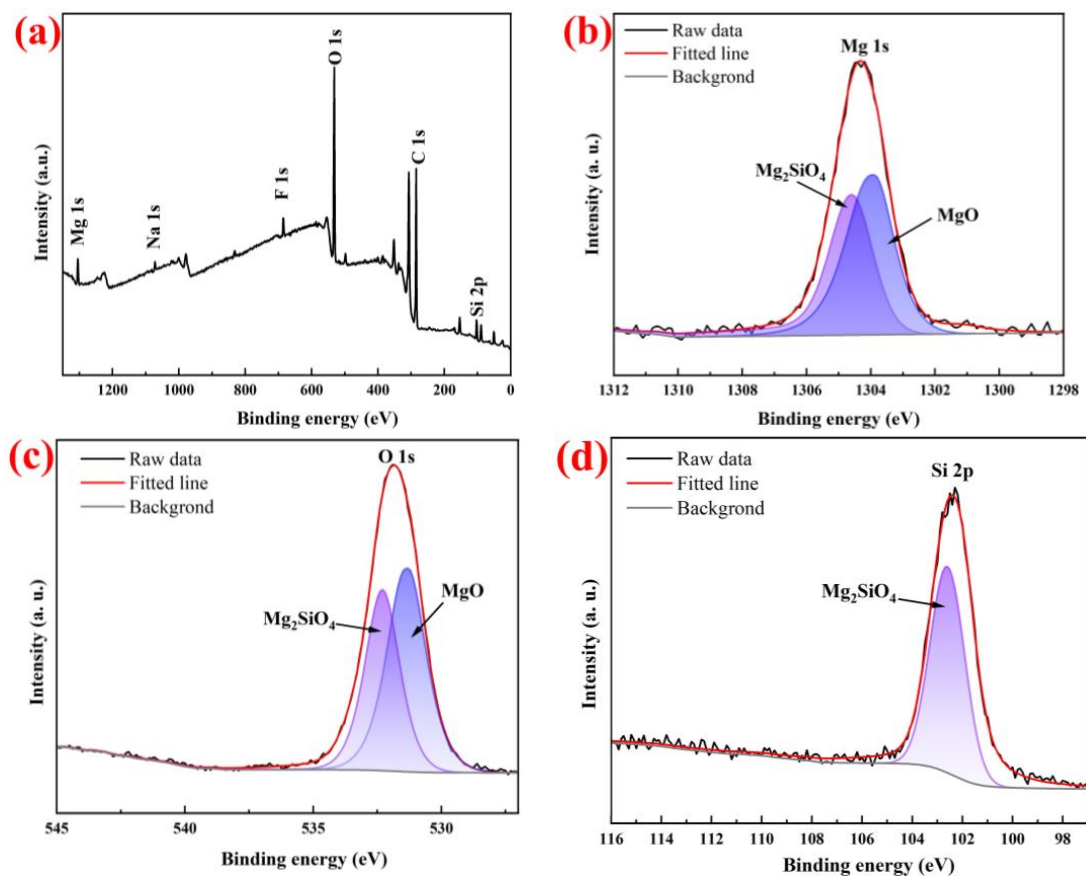

Figure 4. XPS spectra of 450 V MAO coating: (**a**) survey spectrum; high-resolution spectra of (**b**) Mg 1s, (**c**) O 1s, and (**d**) Si 2p.

3.2. Corrosion Behavior

The representative polarization curves of the specimens are plotted in Figure 5, and the electrochemical parameters fitted by Tafel extrapolation are listed in Table 2. Compared with the Mg substrate without MAO treatment, the corrosion current density of the specimens after MAO treatment at 400 V, 425 V, 450 V, and 475 V was reduced by about three, four, six, and two orders of magnitude, revealing a significant improvement in corrosion resistance. Moreover, the corrosion potential of the MAO specimens decreases and then increases with increasing MAO voltage, which indicates that the corrosion tendency is the lowest at a voltage of 450 V. Generally, the corrosion resistance of the alloy is significantly improved with increases in voltage of up to 450 V from both the thermodynamic and dynamic perspectives.
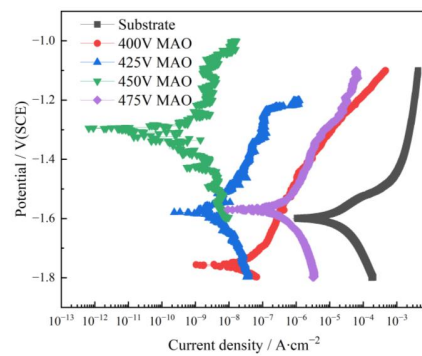
Figure 5. Potentiodynamic polarization curves of the substrate and MAO-treated specimens in SBF.

Table 2. Electrochemical parameters of the specimens fitted according to Figure 5.

Specimen	Substrate	400 V	425 V	450 V	475 V
E_{corr} (V)	-1.59 ± 0.02	-1.76 ± 0.02	-1.58 ± 0.01	-1.29 ± 0.02	-1.57 ± 0.01
I_{corr} (A/cm^2)	$2.67 \pm 0.13 \times 10^{-5}$	$2.31 \pm 0.05 \times 10^{-8}$	$5.23 \pm 0.22 \times 10^{-9}$	$2.75 \pm 0.36 \times 10^{-10}$	$8.23 \pm 0.15 \times 10^{-7}$

EIS measurements were introduced to explore the corrosion behavior of the treated and untreated GZ31K Mg alloys. The Nyquist, bode, and phase plots of the specimens are presented in Figure 6, as well as the corresponding equivalent circuit models. The impedance data are fitted and shown in Table 3.
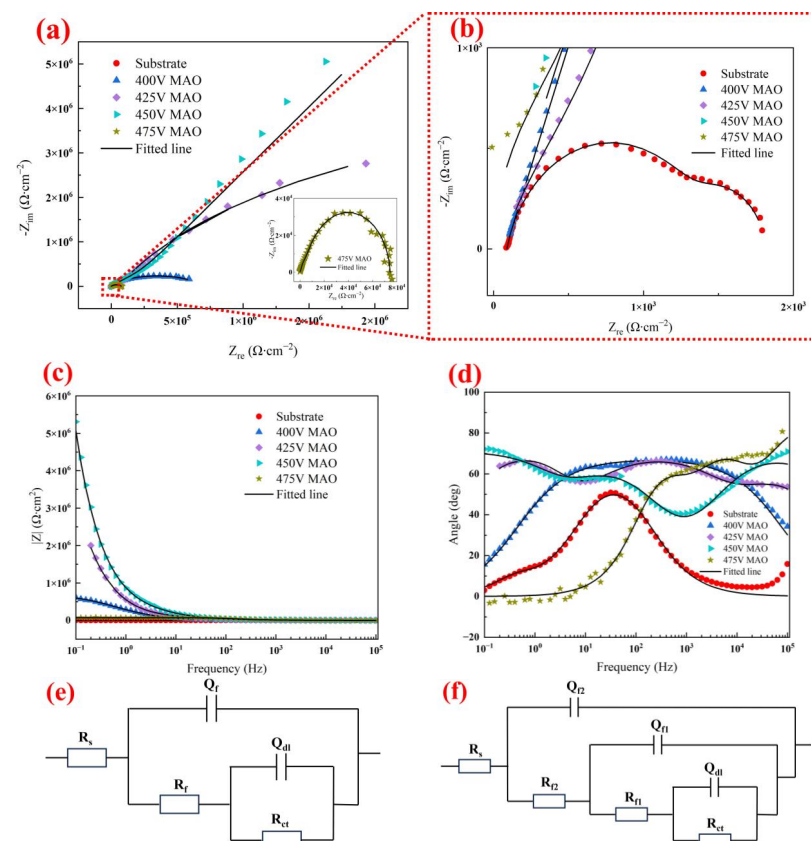

Figure 6. Nyquist diagrams (**a**,**b**), bode diagram (**c**), and phase diagram (**d**) of GZ31K Mg alloy matrix and micro-arc oxide layer under different voltages and their equivalent circuit model: (**e**) Substrate and 400 V MAO, (**f**) 425 V MAO, 450 V MAO, and 475 V MAO.

Table 3. Fitting results of electrochemical parameters obtained from EIS.

Specimen	Substrate	400 V MAO	425 V MAO	450 V MAO	475 V MAO
R_s /$\Omega \cdot cm^2$	89.4	81.0	54.5	78.1	79.3
Y_f/$\Omega^{-1} \cdot cm^{-2} \cdot s^{n}_{f}$	3.08×10^{-5}	6.62×10^{-7}			
n_f	0.835	0.751			
R_f/$\Omega \cdot cm^2$	1.35×10^{3}	1.14×10^{-2}			
Y_{f2}/$\Omega^{-1} \cdot cm^{-2} \cdot s^{n}_{f2}$			1.73×10^{-7}	2.76×10^{-8}	1.48×10^{-7}
n_{f2}			0.762	0.801	0.763
R_{f2}/$\Omega \cdot cm^2$			2.52×10^{3}	1.78×10^{4}	2.11×10^{5}
Y_{f1}/$\Omega^{-1} \cdot cm^{-2} \cdot s^{n}_{f1}$			88.5×10^{-8}	1.41×10^{-7}	8.53×10^{-8}
n_{f1}			0.79	0.77	0.81
R_{f1}/$\Omega \cdot cm^2$			3.21×10^{5}	6.23×10^{5}	6.49×10^{6}
Y_{dl}/$\Omega^{-1} \cdot cm^{-2} \cdot s^{n}$	9.85×10^{-4}	4.18×10^{-7}	1.54×10^{-7}	1.18×10^{-7}	2.27×10^{-7}
n	0.892	0.786	0.895	0.823	0.978
R_{ct} /$\Omega \cdot cm^2$	3.71×10^{2}	7.12×10^{5}	1.08×10^{7}	9.34×10^{8}	3.74×10^{5}
R_p /$\Omega \cdot cm^2$	1.72×10^{3}	7.13×10^{5}	1.11×10^{7}	9.35×10^{8}	7.08×10^{6}
Error	5.19×10^{-3}	4.50×10^{-4}	8.12×10^{-4}	8.69×10^{-4}	3.78×10^{-4}

It can be seen in Figure 6a that the 425 V MAO alloy and the 450 V MAO alloy do not show a complete semicircular arc because the charge transfer resistance was much faster than the diffusion rate, and capacitance arcs were not yet been fully formed [16]. The 400 V MAO and the 475 V MAO samples have more complete capacitance arcs. Figure 6b shows the partial magnification of the Nyquist curves, from which it can be seen that the substrate has a complete capacitive arc, but the radius of the capacitive arc is relatively small. Figure 6a shows the Nyquist curve of 475 V MAO in the lower right corner. It can be seen from the figure that the capacitive arc radius of 475 V MAO is larger than that of the matrix. Since the radius of the capacitive arc reflects the corrosion resistance of the specimen, a larger capacitive arc radius implies a lower corrosion rate [32]. The increase in the capacitive arc radius indicates that 450 V MAO has the best corrosion resistance. As seen from the Bode plot in Figure 6c, the impedance modulus of the alloy ($|Z|_f = 0.01$ Hz) gradually increases with an increase in voltage. It has been shown [33] that the MAO coating has a triple constant in the whole frequency range, in which the capacitive loop in the high-frequency region is attributed to the charge transfer at the interface between the substrate and the electrolyte, reflecting the integrity of the film; the mid-frequency capacitive loop is related to the response of the internal dense layer; and the low-frequency loop corresponds to the external porous layer. The magnitude of the impedance modulus in the lowest-frequency region is used as a semi-quantitative index to evaluate the corrosion resistance of the film [32]. Since 450 V MAO has the highest low-frequency impedance modulus (5.72×10^6 $\Omega \cdot cm^2$), it is suggested to have the best corrosion resistance. Generally, the phase angle at high frequencies in the phase diagram is related to the film [34]. As seen in Figure 6d, the phase angle diagram of the micro-arc oxidized film shows a more stable trend compared to the substrate, where the 475 V MAO specimen has the largest phase angle (80°) at high frequencies, indicating that 475 V MAO has the best integrity.

In order to understand the corrosion process of the film, the impedance data were fitted by the corresponding equivalent circuit models, as shown in Figure 6e,f. R_s is the solution resistance, Q_{dl} is the double-layer constant phase angle element, R_{ct} is the charge transfer resistance, Q_f is the constant phase angle element of oxidation film, and R_f is the film resistance. Moreover, the polarization resistance (R_p) was calculated based on Equation (1), and a higher R_p represents better corrosion resistance [35]. Figure 6e shows the equivalent circuit for the Mg alloy substrate, where Q_f represents the capacitance of the corrosion product film, and Q_{dl} represents the capacitance between the oxide film/ 400 V MAO coating and the Mg alloy substrate, respectively, due to the thin film in the 400 V MAO alloy, which has the same equivalent circuit model as the Mg alloy matrix. Q_{f2}

and Q_{f1} represent the capacitance of the porous outer and dense inner layers, respectively, and the corresponding equivalent circuit fitting data are shown in Table 3.

In addition, R_{f1} is related to the denseness, microporosity and thickness of the inner layer, while R_{f2} is related to the outer layer. From the data in Table 3, it can be seen that with the increase in voltage, R_{f1} and R_{f2} gradually increase, indicating that the thickness of the film increases. Usually, R_{ct} is considered an important index for evaluating the corrosion resistance of the film, which is positively correlated with the corrosion capacity. The fitting results show that the MAO coating has a higher R_{ct} and lower Q_{dl} than the untreated GZ31K Mg alloy substrate, where the 450 V MAO has the highest R_{ct} (9.34×10^8 $\Omega \cdot cm^2$) and the lowest Q_{dl} (1.18×10^{-7} $\Omega^{-1} \cdot cm^{-2} \cdot s$), which suggests that the layer has the best corrosion resistance.

$$R_p = R_{ct} + R_f \tag{1}$$

In summary, with the increase in voltage, the corrosion resistance increases first and then decreases, and the highest corrosion resistance can be increased by six orders of magnitude. On the one hand, when the voltage is low, there are more micropores on the surface; the porosity decreases with the increase in voltage, but microcracks appear. It has been reported that pores and microcracks in the coating serve as conductive pathways for ions [6]. The coating/substrate interface acts as a good barrier to inhibit the penetration of aggressive electrolytes onto the metal surface. It can be seen from Figure 2 that the thickness of the film gradually increases with the increase in voltage, so when the voltage rises to 450 V, even if there are microcracks, because the film is thicker and the interface between the coating and the matrix is relatively compact, it is difficult for the ions in the corrosion medium to reach and corrode the surface of the substrate. However, when the voltage continues to rise to 475 V, although the film is thicker, many large pores are distributed in the film, which allows for the ions in the corrosive medium to reach the substrate surface. On the other hand, it can be seen from Figure 5 that as the voltage increases, the E_{corr} of the MAO-coated sample first increases and then decreases, which may be caused by the porous surface indirectly affecting the equilibrium change in the anode and cathodic reactions on the surface. In addition, the anode of the polarization curve represents the dissolution of the magnesium matrix, while the cathodic polarization curve represents the hydrogen evolution reaction [36]. When the voltage is 425 V and 450 V, the anodic polarization curve of the MAO coating shows significant passivation behavior, revealing that the anodic reaction is further inhibited. Further comparing the corrosion resistance of the GZ31K Mg alloy matrix and MAO coating under different voltages through EIS, in general, with the increase in voltage, the thickness of the film increases, and the R_p also first increases and then decreases, so the corrosion resistance of the 450 V MAO sample is apparently improved.

Figure 7 shows the surface and cross-sectional morphologies of the substrate and MAO-treated specimens after immersion in SBF for 128 h to study the corrosion mode. As can be seen from Figure 7b–e, the typical microporous structure of the MAO coating is still visible, indicating that the corrosion was not severe and that some of the pores were plugged with corrosion products. In addition, some cracks appear on the surface. The cracks on the surface of the coating are caused by the corrosive medium penetrating through the pores; after the corrosive medium comes into contact with the Mg alloy substrate, a corrosion reaction occurs, and the resulting corrosion products block the pores and cause stresses, resulting in cracks in the coating [28]. There are also white, bright, aggregated particles on the surface of the film, distributed near the micropores and cracks. This is mainly because the destruction of the oxide film layer and the appearance of cracks reduce the densification of the specimen surface, and the corrosion medium enters the Mg alloy substrate through the micropores, generating a relatively homogeneous layer of products.
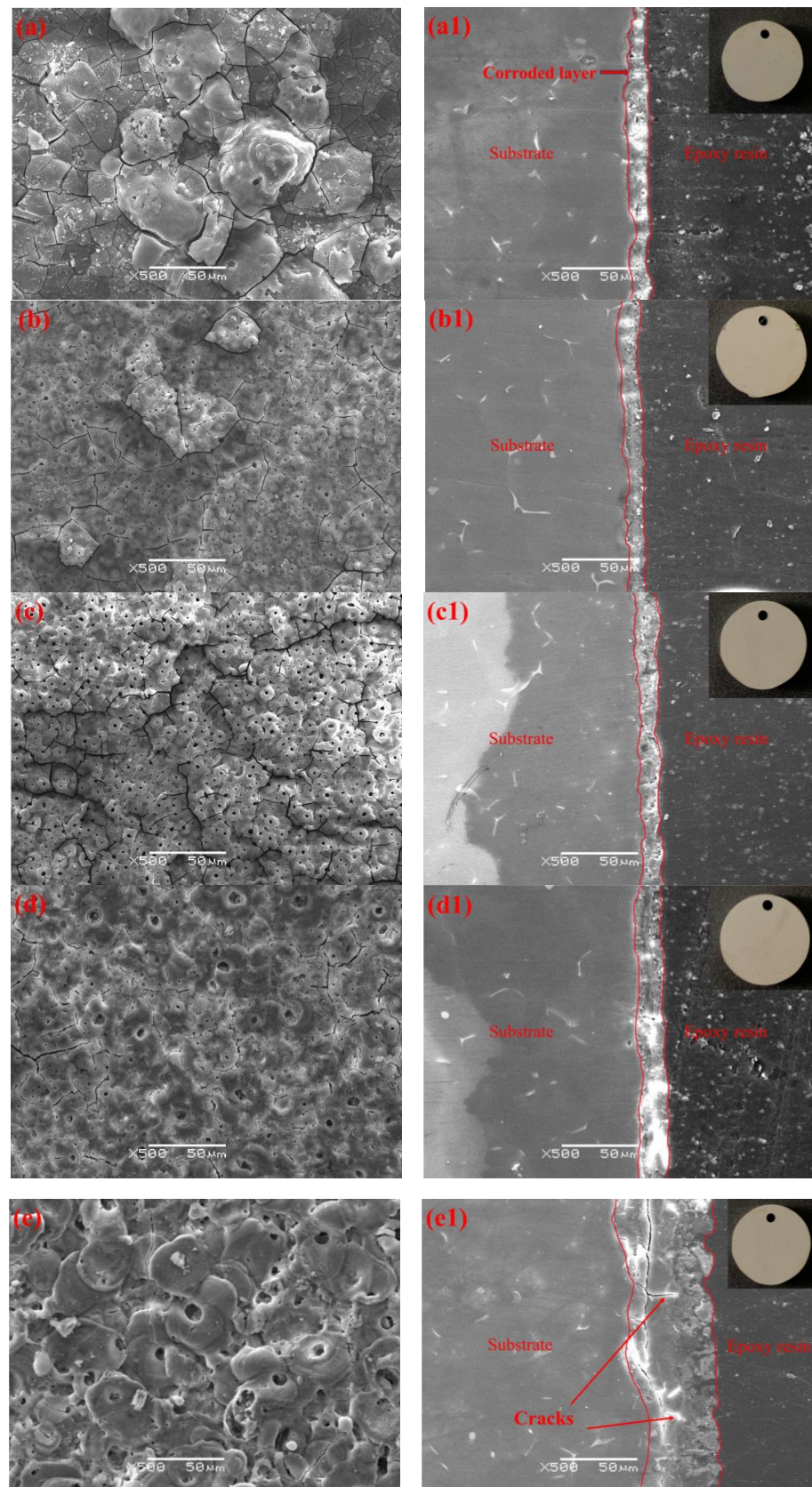
Figure 7. Surface and cross-section images of the substrate and MAO-treated specimens after immersion in SBF for 128 h (**a**,**a1**) substrate, (**b**,**b1**) 400 V MAO, (**c**,**c1**) 425 V MAO, (**d**,**d1**) 450 V MAO, and (**e**,**e1**) 475 V MAO.

From the cross-sections in Figure 7(a1), it can be seen that a layer of corrosion products with a thickness of ~10 μm is formed on the substrate after immersion. Figure 7(b1–d1) show that the sum of the thickness of the MAO coating and its surface corrosion products gradually increases, which is mainly attributed to the thicker MAO coating. The loose and porous part of the MAO coating is filled with corrosion products with a uniform corrosion characteristic, especially 450 V MAO. However, when the voltage was increased to 475 V, as shown in Figure 7(e1), deeper cracks were clearly produced in its cross-section and many bright corrosion products were distributed on the surface of the substrate, indicating that the corrosion products reached the surface of the substrate through the cracks. The macroscopic surfaces of the specimens after removing the corrosion products are shown in Figure 7(a1–e1). The corrosion process is relatively uniform for both substrate and MAO-treated specimens, which is desired for biomedical Mg alloys because the mechanical integrity can be maintained during service without localized corrosion. The main reason for this is likely that the corrosion potential of the MAO coating (MgO and Si_2MgO_4) is close to that of the GZ31K substrate.

It was reported that the film thickness increases, along with the number of cracks, as the voltage increases [37]. Although the coating thickness increases, due to cracks and breakdowns, the corrosive medium enters the surface of the alloy through the cracks to erode the substrate, and the corrosion current density increases, thus reducing the corrosion resistance. In addition, at some point, when the voltage exceeds a critical value, the coating cannot be further optimized and instead will peel off and roughen. However, the corrosion resistance of the MAO coatings increases and then decreases with increasing voltage in this work. The experiments showed that with the increase in voltage, the growth of the MAO coating was accelerated and the thickness of the film increased with the appearance of an inner layer, dense layer, and loose layer. Due to the thicker film layer, the cracks generated during the MAO process had little effect on the corrosion resistance of the alloy [23]. However, when the voltage continues to increase to a critical value, cracks, as well as the effect of micropores, reduce the corrosion resistance. As a consequence, the voltage parameter during the MAO treatment of Mg alloys plays a significant role in the corrosion resistance of the coating, and needs to be controlled and optimized.

It is well known that the applied voltage is one of the most important factors influencing the MAO process. In this study, when the applied voltage is 400–450 V, the surface aperture of the MAO coating is smaller and the number of holes is higher. When the applied voltage is 450–475 V, the size of the holes is obviously larger and their number is greatly reduced. In summary, the microstructure of the coating surface is optimal at 450 V applied voltage. In addition, the corrosion resistance of the MAO coating was characterized by electrochemical experiments. It can also be seen that the corrosion current of the samples decreases when the applied voltage is lower than 450 V, but increases with an applied voltage of higher than 450 V, showing the superior corrosion protection provided by the 450 V MAO coating. The corrosion resistance of the coatings is affected by many factors, such as the film composition, thickness, and microstructure. For example, the 400 V MAO coating shows the worst corrosion resistance among all coated samples because of its lower thickness. In addition, the corrosion protection is found to be proportional to the coating thickness. A thicker coating is beneficial for the improvement in corrosion resistance. Moreover, the integrity of the MAO coatings also greatly affects the corrosion resistance. For instance, the 475 V MAO coating, despite having a larger thickness, had a worse corrosion resistance than the 450 V MAO coating. This is probably due to the large micropores and cracks present inside the coatings, which allow for more corrosive medium to penetrate into the coating, thus reducing its corrosion resistance. During the MAO process, we can select the appropriate electrolyte additives to improve the performance of the film or to achieve self-sealing holes [38]. Therefore, the many characterization experiments proved that the alloy exhibits good corrosion resistance and still maintains uniform corrosion at 450 V applied voltage.

4. Conclusions

In this study, micro-arc oxidation treatments were carried out on Mg-3Gd-1Zn-0.4Zr alloys for surface modification. The microstructures, phases, and corrosion behaviors of MAO-coated Mg alloys were investigated, and the main conclusions are listed as follows:

(1) The main phase compositions of MAO coatings were MgO and Mg_2SiO_4. With the increase in voltage, the porosity in the MAO coating decreases and the film becomes thicker.

(2) The corrosion current density decreases and then increases, the radius of the capacitive arc increases and then decreases, and the impedance modulus ($|Z|_f = 0.01$ Hz) increases and then decreases with the increase in voltage. Meanwhile, the polarization resistance (R_p) also increases and then decreases. Due to the increase in thickness and the decrease in porosity, the anodic reaction is suppressed to a large extent, and the corrosion resistance is improved by six orders of magnitude under 450 V voltage compared to the substrate without MAO treatment.

(3) The GZ31K alloy in SBF shows uniform corrosion characteristics, and after MAO treatment, the specimens still exhibit a uniform corrosion mode, indicating that MAO treatment does not change the corrosion characteristics of the substrate, which is the desired performance for biodegradable implanted applications.

Author Contributions: Conceptualization, X.G. and X.Z.; methodology, X.G.; software, X.G.; validation, X.G. and Q.D.; formal analysis, X.G. and Q.D.; investigation, X.G.; resources, X.G.; data curation, X.G. and X.Z.; writing—original draft preparation, X.G. and Q.D.; writing—review and editing, X.Z.; visualization, X.G. and Q.D.; supervision, X.Z.; project administration, X.Z.; funding acquisition, X.Z. All authors have read and agreed to the published version of the manuscript.

Data Availability Statement: The data presented in this study are available on request from the corresponding author. The data are not publicly available due to privacy.

Conflicts of Interest: The authors declare no conflict of interest.

References

1. Liu, D.X.; Yang, D.L.; Li, X.L.; Hu, S.W. Mechanical properties, corrosion resistance and biocompatibilities of degradable Mg-RE alloys: A review. *J. Mater. Res. Technol.* **2019**, *8*, 1538–1549. [CrossRef]
2. Meysam, N.A.; Abolfazl, Z.; Oluwole, K.B.; Bankole, I.O. A review of current challenges and prospects of magnesium and its alloy for bone implant applications. *Prog. Biomater.* **2022**, *11*, 1–26. [CrossRef]
3. Nie, Y.J.; Dai, J.W.; Li, X.; Zhang, X.B. Recent developments on corrosion behaviors of Mg alloys with stacking fault or long period stacking ordered structures. *J. Magnes. Alloys* **2021**, *9*, 1123–1146. [CrossRef]
4. Lin, Z.S.; Wang, T.L.; Yu, X.M.; Sun, X.T.; Yang, H.Z. Functionalization treatment of micro-arc oxidation coatings on magnesium alloys: A review. *J. Alloys Compd.* **2021**, *879*, 160453. [CrossRef]
5. Sankara Narayanan, T.S.N.; Park, I.S.; Lee, M.H. Strategies to improve the corrosion resistance of microarc oxidation (MAO) coated magnesium alloys for degradable implants: Prospects and challenges. *Prog. Mater. Sci.* **2014**, *60*, 1–71. [CrossRef]
6. Lim, T.S.; Ryu, H.S.; Hong, S.H. Electrochemical corrosion properties of CeO2-containing coatings on AZ31 magnesium alloys prepared by plasma electrolytic oxidation. *Corros. Sci.* **2012**, *62*, 104–111. [CrossRef]
7. Pan, Y.K.; He, S.Y.; Wang, D.G.; Huang, D.L.; Zheng, T.T.; Wang, S.Q.; Dong, P.; Chen, C. In vitro degradation and electrochemical corrosion evaluations of microarc oxidized pure Mg, Mg–Ca and Mg–Ca–Zn alloys for biomedical applications. *Mater. Sci. Eng. C* **2015**, *47*, 85–96. [CrossRef]
8. Toorani, M.; Aliofkhazraei, M. Review of electrochemical properties of hybrid coating systems on Mg with plasma electrolytic oxidation process as pretreatment. *Surf. Interfaces* **2019**, *14*, 262–295. [CrossRef]
9. Chen, C.A.; Jian, S.Y.; Lu, C.H.; Lee, C.Y.; Aktuğ, S.L.; Ger, M.D. Evaluation of microstructural effects on corrosion behavior of AZ31B magnesium alloy with a MAO coating and electroless Ni-P plating. *J. Mater. Res. Technol.* **2020**, *9*, 13902–13913. [CrossRef]
10. Wu, W.X.; Wang, W.P.; Lin, H.C. A study on corrosion behavior of micro-arc oxidation coatings doped with 2-aminobenzimidazole loaded halloysite nanotubes on AZ31 magnesium alloys. *Surf. Coat. Technol.* **2021**, *416*, 127116. [CrossRef]

11. Waizy, H.; Diekmann, J.; Weizbauer, A.; Reifenrath, J.; Bartsch, I.; Neubert, V.; Schavan, R.; Windhagen, H. In vivo study of a biodegradable orthopedic screw (MgYREZr-alloy) in a rabbit model for up to 12 months. *J. Biomater. Appl.* **2013**, *28*, 667–675. [CrossRef]

12. Zhuang, J.J.; Guo, Y.Q.; Xiang, N.; Xiong, Y.; Hu, Q.; Song, R.G. A study on microstructure and corrosion resistance of ZrO₂-containing PEO coatings formed on AZ31 Mg alloy in phosphate-based electrolyte. *Appl. Surf. Sci.* **2015**, *357*, 1463–1471. [CrossRef]

13. Lin, X.; Tan, L.L.; Zhang, Q.; Yang, K.; Hu, Z.Q.; Qiu, J.H.; Cai, Y. The in vitro degradation process and biocompatibility of a ZK60 magnesium alloy with a forsterite-containing micro-arc oxidation coating. *Acta Biomater.* **2013**, *9*, 8631–8642. [CrossRef]

14. Liang, J.; Bala Srinivasan, P.; Blawert, C.; Dietzel, W. Influence of chloride ion concentration on the electrochemical corrosion behaviour of plasma electrolytic oxidation coated AM50 magnesium alloy. *Electrochim. Acta* **2010**, *55*, 6802–6811. [CrossRef]

15. Wang, L.Q.; Zhou, J.S.; Liang, J.; Chen, J.M. Corrosion mechanism of plasma electrolytic oxidation coated magnesium alloy with laser surface melting pretreatment. *J. Electrochem. Soc.* **2014**, *161*, C20–C24. [CrossRef]

16. Huang, Y.W.; Sun, X.L.; Song, J.L.; Chen, J.H.; Gao, J.; Xiao, K. Study on corrosion protection behavior of magnesium alloy/micro-arc oxidation coating in neutral salt spray environment. *Int. J. Electrochem. Sci.* **2023**, *18*, 100179. [CrossRef]

17. Cui, X.J.; Lin, X.Z.; Liu, C.H.; Yang, R.S.; Zheng, X.W.; Gong, M. Fabrication and corrosion resistance of a hydrophobic micro-arc oxidation coating on AZ31 Mg alloy. *Corros. Sci.* **2015**, *90*, 402–412. [CrossRef]

18. Chen, J.X.; Zhang, Y.; Ibrahim, M.; Etim, I.P.; Tan, L.; Yang, K. In vitro degradation and antibacterial property of a copper-containing micro-arc oxidation coating on Mg-2Zn-1Gd-0.5Zr alloy. *Colloids Surf. B* **2019**, *179*, 77–86. [CrossRef] [PubMed]

19. Fischerauer, S.F.; Kraus, T.; Wu, X.; Tangl, S.; Sorantin, E.; Hänzi, A.C.; Löffler, J.F.; Uggowitzer, P.J.; Weinberg, A.M. In vivo degradation performance of micro-arc-oxidized magnesium implants: A micro-CT study in rats. *Acta Biomater.* **2013**, *9*, 5411–5420. [CrossRef] [PubMed]

20. Wolters, L.; Besdo, S.; Angrisani, N.; Wriggers, P.; Hering, B.; Seitz, J.M.; Reifenrath, J. Degradation behaviour of LAE442-based plate–screw-systems in an in vitro bone model. *Mater. Sci. Eng. C* **2015**, *49*, 305–315. [CrossRef] [PubMed]

21. Yin, S.Q.; Duan, W.C.; Liu, W.H.; Zhang, Z.Q. Influence of specific second phases on corrosion behaviors of Mg-Zn-Gd-Zr alloys. *Corros. Sci.* **2019**, *166*, 108419. [CrossRef]

22. Geng, X.; Jiang, J.H.; Zhang, X.B. Corrosion Behavior of Mg-xGd-1Zn-0.4Zr Alloys with Different Gd Additions for Biomedical Application. *Metals* **2022**, *12*, 1763. [CrossRef]

23. Qian, B.Y.; Miao, W.; Qiu, M. Influence of Voltage on the Corrosion and Wear Resistance of Micro-Arc Oxidation Coating on Mg–8Li–2Ca Alloy. *Acta Metall. Sin.* **2019**, *32*, 194–204. [CrossRef]

24. Li, H.Z.; Wang, Y.F.; Geng, J.J.; Li, S.L.; Chen, Y.N. Study on Microstructure and Properties of Black Micro-Arc Oxidation Coating on AZ31 Magnesium Alloy by Orthogonal Experiment. *Materials* **2022**, *15*, 8755. [CrossRef] [PubMed]

25. Yu, Y.D.; Kuang, S.Z.; Li, J. Influence of Applied Voltage and Film-Formation Time on Microstructure and Corrosion Resistance of Coatings Formed on Mg-Zn-Zr-Ca Bio-magnesium Alloy. *JOM* **2015**, *67*, 2133–2144. [CrossRef]

26. Zhang, X.B.; Dai, J.W.; Zhang, R.F.; Ba, Z.X.; Birbilis, N. Corrosion behavior of Mg–3Gd–1Zn–0.4Zr alloy with and without stacking faults. *J. Magnes. Alloys* **2019**, *7*, 240–248. [CrossRef]

27. Song, D.D.; Wan, H.X. Key factor for the corrosion resistance of MAO coating on Mg alloy. *Mater. Chem. Phys.* **2023**, *305*, 127963. [CrossRef]

28. Barati Darband, G.; Aliofkhazraei, M.; Hamghalam, P.; Valizade, N. Plasma electrolytic oxidation of magnesium and its alloys: Mechanism, properties and applications. *J. Magnes. Alloys* **2017**, *5*, 74–132. [CrossRef]

29. Li, Y.; Lu, F.; Li, L.L.; Zhu, W.J.; Pan, H.B.; Tan, G.X.; Lao, Y.H.; Ning, C.Y.; Ni, G.X. Corrosion mechanism of micro-arc oxidation treated biocompatible AZ31 magnesium alloy in simulated body fluid. *Prog. Nat. Sci.—Mater.* **2014**, *24*, 516–522. [CrossRef]

30. Yagi, S.; Kuwabara, K.; Fukuta, Y.; Kubota, K.; Matsubara, E. Formation of self-repairing anodized film on ACM522 magnesium alloy by plasma electrolytic oxidation. *Corros. Sci.* **2018**, *73*, 188–195. [CrossRef]

31. Li, Z.J.; Jing, X.Y.; Yuan, Y.; Zhang, M.L. Composite coatings on a Mg–Li alloy prepared by combined plasma electrolytic oxidation and sol–gel techniques. *Corros. Sci.* **2012**, *63*, 358–366. [CrossRef]

32. Dong, Q.S.; Jia, Y.Q.; Ba, Z.X.; Tao, X.W.; Wang, Z.Z.; Xue, F.; Bai, J. Exploring the corrosion behavior of Mn-implanted biomedical Mg. *J. Alloys Compd.* **2021**, *873*, 159739. [CrossRef]

33. Dong, Q.S.; Zhou, X.X.; Feng, Y.J.; Qian, K.; Liu, H.; Lu, M.M.; Chu, C.L.; Xue, F.; Bai, J. Insights into self-healing behavior and mechanism of dicalcium phosphate dihydrate coating on biomedical Mg. *Bioact. Mater.* **2021**, *6*, 158–168. [CrossRef] [PubMed]

34. Saady, A.; Rais, Z.; Benhiba, F.; Salim, R.; Ismaily, A.K.; Arrousse, N.; Elhajjaji, F.; Taleb, M.; Jarmoni, K.; Kandri, R.Y.; et al. Chemical, electrochemical, quantum, and surface analysis evaluation on the inhibition performance of novel imidazo [4,5-b] pyridine derivatives against mild steel corrosion. *Corros. Sci.* **2021**, *189*, 109621. [CrossRef]

35. Xie, J.S.; Wang, L.L.; Zhang, J.H.; Lu, L.W.; Zhang, Z.; He, Y.Y.; Wu, R.Z. Developing new Mg alloy as potential bone repair material via constructing weak anode nano-lamellar structure. *J. Magnes. Alloys* **2023**, *11*, 154–175. [CrossRef]

36. Xue, K.; Tan, P.H.; Zhao, Z.H.; Cui, L.Y.; Kannan, M.B.; Li, S.Q.; Liu, C.B.; Zou, Y.H.; Zhang, F.; Chen, Z.Y.; et al. In vitro degradation and multi-antibacterial mechanisms of β-cyclodextrin@curcumin embodied Mg(OH)₂/MAO coating on AZ31 magnesium alloy. *J. Mater. Sci. Technol.* **2023**, *132*, 179–192. [CrossRef]

37. Lu, J.P.; Cao, G.P.; Quan, G.F.; Wang, C.; Zhuang, J.J.; Song, R.G. Effects of Voltage on Microstructure and Corrosion Resistance of Micro-arc Oxidation Ceramic Coatings Formed on KBM10 Magnesium Alloy. *J. Mater. Eng. Perform.* **2018**, *27*, 147–154. [CrossRef]
38. Tang, M.Q.; Shao, Y.F.; Feng, Z.Q.; Wang, W.; Li, G.; Yan, Z.W.; Zhang, R.Z. Self-sealing Microarc Oxidation Coating Mainly Containing ZrO2 and Nano Mg2Zr5O12 on AZ91D Mg Alloy. *Int. J. Electrochem. Sci.* **2020**, *15*, 12447–12461. [CrossRef]